Analysis of Mir Reentry Breakup

11 February 2003

Prepared by

R. G. Stern
Imagery Programs Division
National Systems Group

Prepared for

SPACE AND MISSILE SYSTEMS CENTER
AIR FORCE SPACE COMMAND
2430 E. El Segundo Boulevard
Los Angeles Air Force Base, CA 90245

Systems Planning & Engineering Group

APPROVED FOR PUBLIC RELEASE;
DISTRIBUTION UNLIMITED

THE AEROSPACE CORPORATION
El Segundo, California

20040317 136

John R. Edwards
SMC/AXF

REPORT DOCUMENTATION PAGE

1. REPORT DATE (DD-MM-YYYY) 11-02-2003	2. REPORT TYPE	3. DATES COVERED (From - To)

4. TITLE AND SUBTITLE
Analysis of Mir Reentry Breakup

5a. CONTRACT NUMBER
F04701-00-C-0009

5b. GRANT NUMBER

5c. PROGRAM ELEMENT NUMBER

6. AUTHOR(S)
Richard G. Stern

5d. PROJECT NUMBER

5e. TASK NUMBER

5f. WORK UNIT NUMBER

7. PERFORMING ORGANIZATION NAME(S) AND ADDRESS(ES)

The Aerospace Corporation
Engineering and Technology Group
El Segundo, CA 90245-4691

8. PERFORMING ORGANIZATION REPORT NUMBER

TR-2003(8506)-1

9. SPONSORING / MONITORING AGENCY NAME(S) AND ADDRESS(ES)
Space and Missile Systems Center
Air Force Space Command
2450 E. El Segundo Blvd.
Los Angeles Air Force Base, CA 90245

10. SPONSOR/MONITOR'S ACRONYM(S)
SMC

11. SPONSOR/MONITOR'S REPORT NUMBER(S)
SMC-TR-04-05

12. DISTRIBUTION/AVAILABILITY STATEMENT

Approved for public release; distribution unlimited.

13. SUPPLEMENTARY NOTES

14. ABSTRACT
Analysis of the CNN video of the Mir reentry, which was generated and supplied by Hugh Williams, was performed. The analysis determined how and when the space station's individual modules mechanically separated from each other. Also, the subsequent time and location of the aerothermal breakup (melting) of several of the modules was established. The aerothermal breakup was consistent with numerous satellite reentries studied by the author.

15. SUBJECT TERMS
Atmospheric Mir Reentry, Reentry Breakup, Aerothermal Heating

16. SECURITY CLASSIFICATION OF:			17. LIMITATION OF ABSTRACT	18. NUMBER OF PAGES	19a. NAME OF RESPONSIBLE PERSON Richard G. Stern
a. REPORT UNCLASSIFIED	b. ABSTRACT UNCLASSIFIED	c. THIS PAGE UNCLASSIFIED		36	19b. TELEPHONE NUMBER (Include area code) (310) 336-4278

Analysis of Mir Reentry Breakup

R. G. Stern

THE AEROSPACE CORPORATION

Analysis of the CNN video of the Mir reentry, which was generated and supplied by Hugh Williams, was performed. Usage of this CNN material does not constitute an implied or expressed endorsement by CNN. The analysis determined how and when the space station's individual modules mechanically separated from each other. Also, the subsequent time and location of the aerothermal breakup (melting) of several of the modules was established. The aerothermal breakup was consistent with numerous satellite reentries studied by the author.

Acknowledgements

➢ Lead Object Tracking Analysis
  ◆ Wayne Hallman (Aerospace)
  ◆ Todd Beltracchi (Aerospace)

➢ MIR Reentry Video from The Fiji Sheraton Resort Hotel
  ◆ Hugh Williams (CNN)

➢ Graphics and Report Preparation
  ◆ Vicky Jackson (Aerospace)

THE AEROSPACE CORPORATION

2

Lead object trajectory analysis was conducted by Drs. Todd Beltracchi and Wayne Hallman. Wayne Hallman provided reentry trajectory reconstruction derived from classified sources (Ref. 8).

Utilizing the trajectory of the lead object and the reentry video provided by Hugh Williams of CNN, it was possible to determine the relative trajectories and characteristics of the objects in the video.

The CNN video utilized in the report was described in the following CNN website:

http://www.cnn.com/2001/TECH/space/03/23/williams.debrief/indes.ht (Ref. 9)

The images taken from the video have been used under license from CNN.

CNN Video Coverage of Mir Aerothermal Breakup of Lead Object

Breakup
GMT 5:46:49
Alt = 38 nm

Vanua Levu

CNN Video Coverage
Start 5:46:36 GMT
End 5:47:05 GMT

Viti Levu

Lau Group

Mir Debris Footprint

□ Breakup
▲ Sheraton Fiji Resort

Latitude (deg)

Longitude (deg)

THE AEROSPACE CORPORATION

3
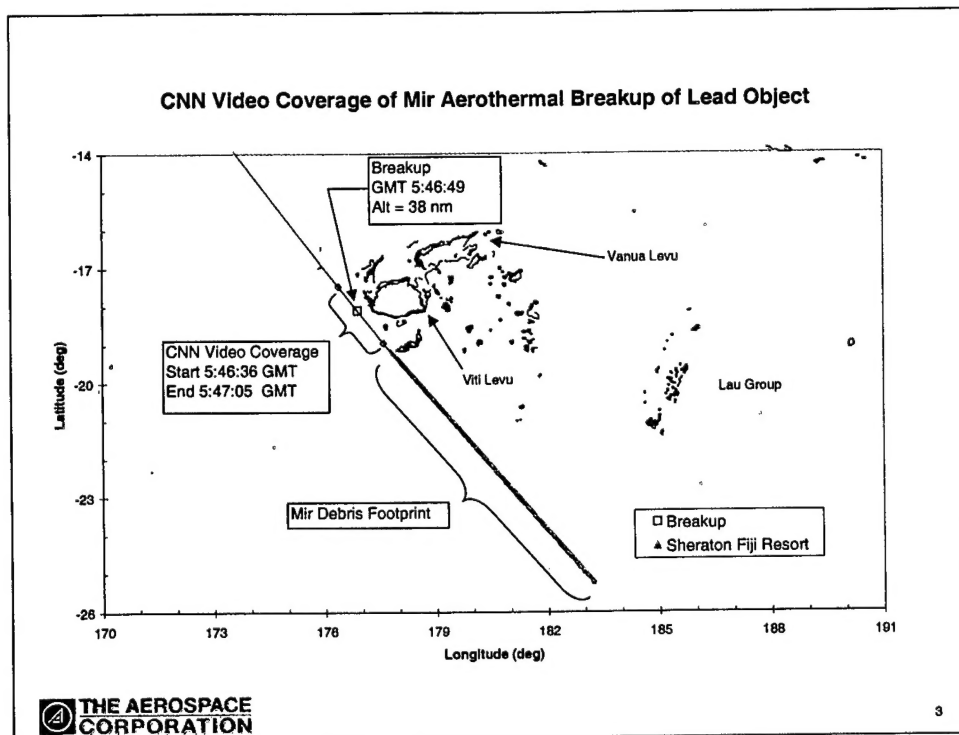
The Mir reentry occurred about 1500 nmi uprange (northwest) of the announced impact area. The reentry could not have been better planned for observation of the reentry breakup process from the western shores of Viti Levu, Fiji Islands. Hugh Williams of CNN was able to video tape about 29 seconds of reentry. The coverage was terminated by extensive cloud cover to the south. The last 10 seconds of coverage was in and out of the clouds. The remaining 19 seconds of coverage could not be better located to provide insight into the nature of the reentry breakup of Mir.

Analysis of MIR Breakup

> Lead Object Tracking

> CNN Video From The Fiji Sheraton Resort Hotel (Hugh Williams)

> Palm Tree at The Fiji Sheraton Resort Hotel

THE AEROSPACE CORPORATION

4

The analysis of the MIR breakup was made possible by having a trajectory of the lead object and the CNN video.

The video covered about 29 seconds of the reentry, the last 10 seconds of which were in and out of cloud cover. Given the limited coverage, the vantage point could not have been better as it revealed the mechanical separation of the compartments comprising MIR and the subsequent aerothermal melting of those compartments.

Having the lead object tracking and the video was not sufficient to do trajectory analysis for the observed objects for several reasons. First, there was no time correlation of the lead object and the video. Second, there was no knowledge of the viewing geometry of the video. Third and last, there was no knowledge of the video's field of view (FOV). A palm tree observed during the video allowed the above difficulties to be circumvented.

Mir Configuration

- ➤ Mir Total Weight at Reentry = 280,000 lbs
- ➤ Mir Components
  - ♦ Core Module : 45,000 lbs
  - ♦ KVANT 1 : 24,000 lbs
  - ♦ KVANT 2: 43,000 lbs
  - ♦ KRYSTALL : 43,000 lbs
  - ♦ SPEKTR : 43,000 lbs
  - ♦ PIRODA : 43,000 lbs
  - ♦ Progress M : 16,000 lbs
  - ♦ Docking Module : 9000 lbs
- ➤ Other Space Station Reentries
  - ♦ SKYLAB (July 1979) Weight = 155,000 lbs
  - ♦ SALYUT7 (Feb 1991) Weight = 81,000 lbs
  - ♦ ISS (2020) Weight = 925,000 lbs
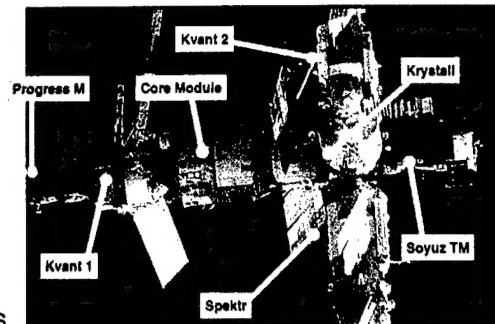
Piroda Module behind Krystall

THE AEROSPACE CORPORATION

5

The MIR configuration at deboost and early reentry are as depicted in the figure with the exception that a Soyuz spacecraft was absent. The inertially stabilized attitude of the vehicle as it approached reentry would place the Progress end of the vehicle pointing upward nearly broadside in the orbit plane. The Progress end would be moving towards a trailing position at 4 degrees per minute. The configuration is aerodynamically stable in an orientation where the Progress end trails.

The configuration would be oscillating with Progress trailing with the Spektr, Kvant2, Krystall and Piroda modules facing into the relative wind. The aerodynamic forces on these modules provide moments during reentry to separate them from the central Core Module, Kvant1 and Progress modules.

What Video Observed

➤ Six to Nine Objects Enter Field Of View
  ◆ Initially Negligible or No Aerothermal Breakup

➤ Mechanical Separation of Two Objects Observed

➤ Aerothermal Breakup of Several Objects

6

Six objects are continually observed in the video and observed until they move out of the camera's field of view (FOV). Additionally, three objects are briefly observed early in the video. No aerothermal melting is observed during early breakup.

The mechanical separation of two objects, assumed to be modules, is observed during early entry.

Late in the video the aerothermal (melting) breakup of the modules still in the field of view is evident.

What Was Derived From Video

➢ Relative Trajectories of 12 Objects
  - Alternate Tracking Could Only Determine Lead Object Trajectory

➢ Ballistic Coefficient of Individual Objects

➢ Initiation Point of Aerothermal Breakup

➢ Breakup Scenario of MIR Space Station

➢ Applicability of Heating Predictions

**THE AEROSPACE
CORPORATION**

7

The analysis of the video provided detailed trajectory data on 12 objects. The classified tracking analysis could not positively identify objects other than the lead object. From the detailed trajectories, ballistic coefficients (Weight/Drag Reference Area) of individual objects could be determined. The time, altitude and velocity of the initiation of aerothermal (melting) breakup was determined from secondary breakup analysis. The trajectory, ballistic coefficient and melting information led to a breakup scenario of the MIR configuration to be surmised. Finally, the melting of the configuration allowed an assessment of heating predictions.
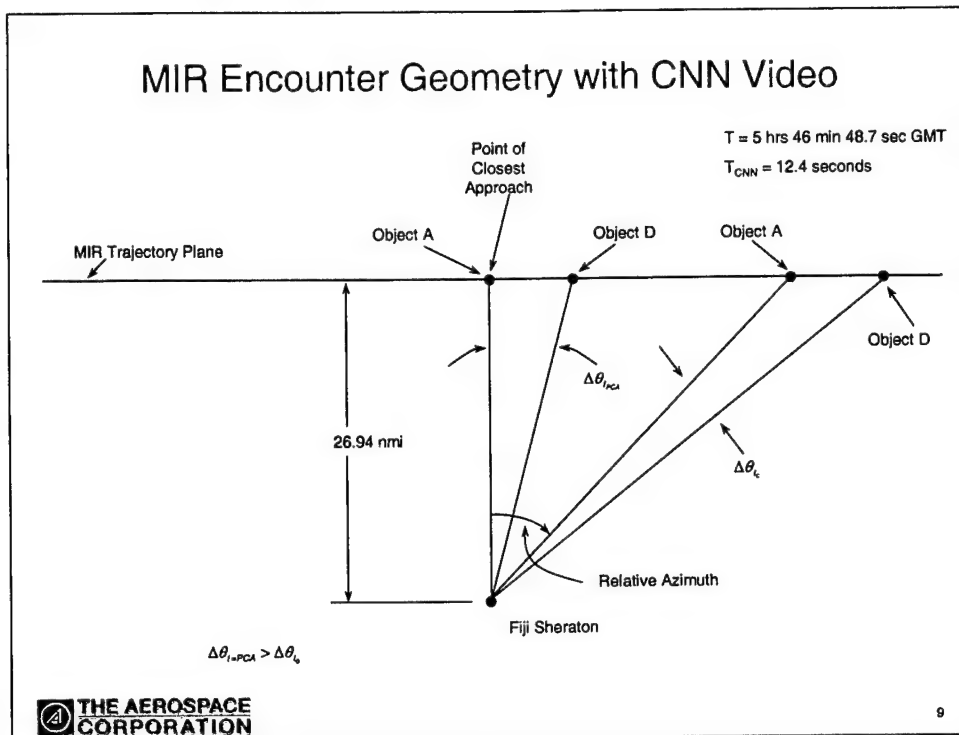
Analytic Approach

➤ Determine Relative Separation of Objects in Terms of CNN Video Field of View
➤ Estimate Point of Closest Approach
➤ Correlate Time With Lead Object Trajectory Point of Closest Approach
➤ Calculate CNN Field of View (FOV) As It Approaches Palm Tree
➤ Using Lead Object Trajectory and Field of View Estimate, Calculate Separation Distances
➤ Iterate to Determine Time Varying Field of View, Revised Separation Distances and Time (Video) of Closest Approach
➤ Determine Ballistic Coefficient From Separation Distance History

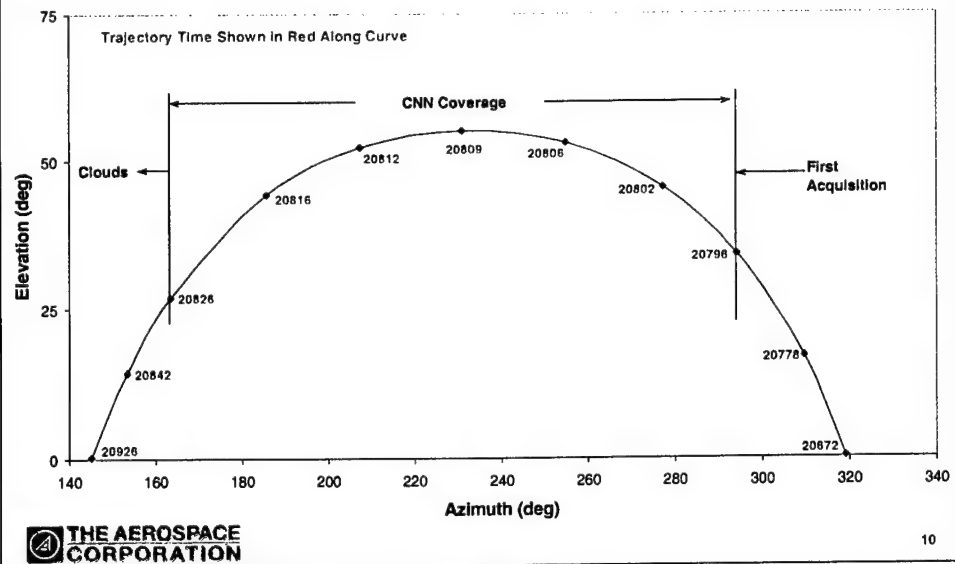**THE AEROSPACE CORPORATION**   8

An outline of the iterative process to determine the relative distances of the objects in the video and their ballistic coefficients is outlined above. Details of the procedure will be provided in subsequent charts.

(1) The separation distances were measured relative to the video screen width (FOV) as a function of time. (An example is provided in Figure 14.)

(2) The point of closest approach is estimated by observing the maximum apparent separation. (Corrupted by changing video FOV.)

(3) Correlate estimated video time of closest approach with lead object trajectory time of closest approach (to Fiji Sheraton Resort Hotel).

(4) The lead object's relative trajectory provides azimuth rate as it approaches the palm tree. The transit time of the lead object as the tree is first observed until it passes the tree, coupled with the azimuth rate yields the angular distance to the tree and hence FOV.

(5) Using the lead object trajectory, the relative azimuths from the camera to the lead object were estimated and hence the distance to the lead object could be determined. An estimate of the FOV and the angular separation of objects in the video enable the calculation of the separation distances of objects.

(6) Steps 2 through 5 are repeated until FOV at all times is determined by evaluating a FOV which is consistent with relative trajectory behavior.

(7) Having determined a separation distance history, the ballistic coefficient history relative to the lead object is established.

MIR Encounter Geometry with CNN Video

The above figure is used to describe some of the geometric aspects of the analytic approach described. The point of closest approach provides a time correlation between the lead object trajectory and the CNN video. At a given time, the lead object's (A) relative geometry to the camera is known. If Object D is trailing Object A by a fixed distance, then the difference in relative azimuth ($\Delta\theta$) will be maximum at the point of closest approach. The relative angular separation of the two objects in the video is dictated by the camera's FOV and the azimuth separation of the objects. The smaller the FOV the greater the apparent separation in the video picture. Also, the larger the separation in azimuth, the larger the apparent separation in the video picture. Thus, once the point of closest approach and FOV history is established, separation distances may be determined.

MIR Azimuth & Elevation From
Sheraton Beach Hotel

Trajectory Time Shown in Red Along Curve

CNN Coverage

Clouds ◄

First
Acquisition

20812   20809   20806

20816

20802

20826

20796

20842

20778

20926

20872

Elevation (deg)

Azimuth (deg)

THE AEROSPACE CORPORATION

10

The time of closest approach for the lead object trajectory is 20808.7 sec GMT
and the CNN video 12.4 seconds from video start. The CNN video first
acquisition occurs at 20796.3 GMT. Based upon the lead object trajectory, the
elevation and azimuth angle as viewed from the video camera vantage point is
provided. The first acquisition of the objects occurs some two minutes after
horizon break at an elevation angle of 35 degrees. The track is lost one-half
minute later in clouds 100 seconds before horizon set. The elevation and
azimuth data as a function of time will be used in calculating separation
distances.

CNN Video Field of View
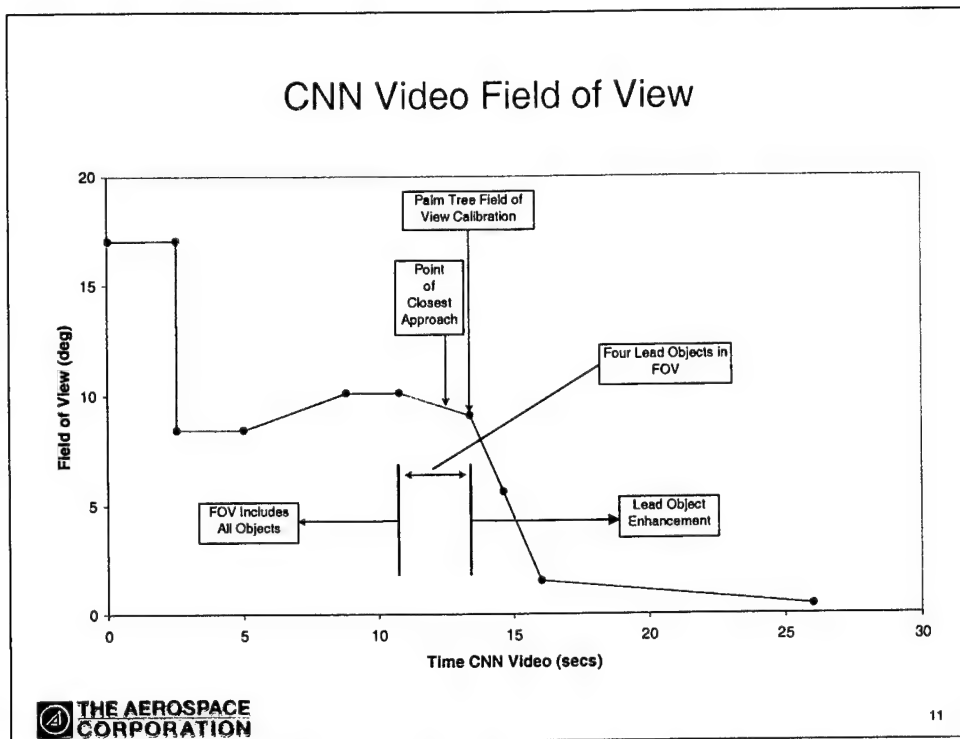
The above figure provides the final iteration and solution of the video's FOV as a function of time. The point of closest approach occurs 12.4 seconds into the video (20808.7 sec GMT). The palm tree FOV calibration occurred at 13.367 seconds (20809.67 sec GMT). The FOV was 16.8 degrees prior to 2.4 seconds at which time the FOV was cut in half (electronically) to 8.4 degrees thereby doubling the magnification. At this time all six major objects are in the FOV. This magnification was held until 5.8 seconds when the FOV linearly increased (magnification decreased) for 3 seconds to 10.08 degrees at which time it was constant for 2 seconds. The object of the camera action to this time was to include all six major objects in the FOV.

At 10.767 seconds, the FOV decreased linearly from 10.08 degrees to 9.054 degrees at 13.367 seconds. Over this interval the lead four major objects are held in the FOV. At 13.367 seconds, the FOV is linearly decreased to 1.5 degrees at 16 seconds. At 16 seconds the FOV linearly was reduced to 0.40 degrees at 26 seconds. The objective after 9.054 seconds was to concentrate upon the lead object as it moved farther from the camera. The FOV decreased increasing the magnification, the result being that excellent coverage of the lead object's aerothermal (melting) breakup was achieved.

The above chart provides data for the final iteration in the determination of the
FOV as the palm tree is approached. The MIR azimuth rate with respect to the
camera position is determined from trajectory data and was relatively insensitive
to the iterative changes in the time of PCA due to the proximity to that point.

Determination of Point of Closest Approach (PCA) and Field of View (FOV) (cont'd)

➢ Procedure for Determination of PCA

   ◆ Measure Relative Spacing History of Six Major Objects in Terms of % Video FOV

   ◆ Estimate Geometric Separation Based on % FOV

   ◆ Note: Relative Positions of Objects (Objects A, D, E & F Maintain Formation)

   ◆ Establish Point of Maximum Angular Separation (PCA) Correcting for Many Changes in FOV

➢ Determine Separation Distance Between Objects Based Upon Viewing Geometry (Range & Azimuth) and Estimated FOV

➢ FOV Changes Will Effect Calculated Separation Distances

   ◆ Objects A, D, E & F Maintain the Same Relative FOV Separations (Therefore Distance)

   ◆ Determine FOV for Times Other Than at 13.367 Seconds by Adjusting to Achieve Constant Separation Distances (A to D, D to E and A to E)

THE AEROSPACE CORPORATION   13

The iterative procedure for determining the PCA as outlined previously was shortened considerably because of the behavior of objects to be identified as A, D, E and F (see Page 23). These objects maintained formation. The ratio of the distances on the video screen from A to D; A to E; A to F; D to E and F remained constant. That indicates that while the angular separation on the video is varying with camera proximity and FOV the actual separation distances are constant. Many iterations therefore can be circumvented with the FOV adjusted from the palm tree calibration point at 13.367 seconds to keep those separation distances constant. The iterations on PCA converged rapidly because of the constraint of constant distances. The FOV determination followed directly as a function of time.

Ratio of Relative Separation Distances from Object A
(Separation Distance A to D = Unity)
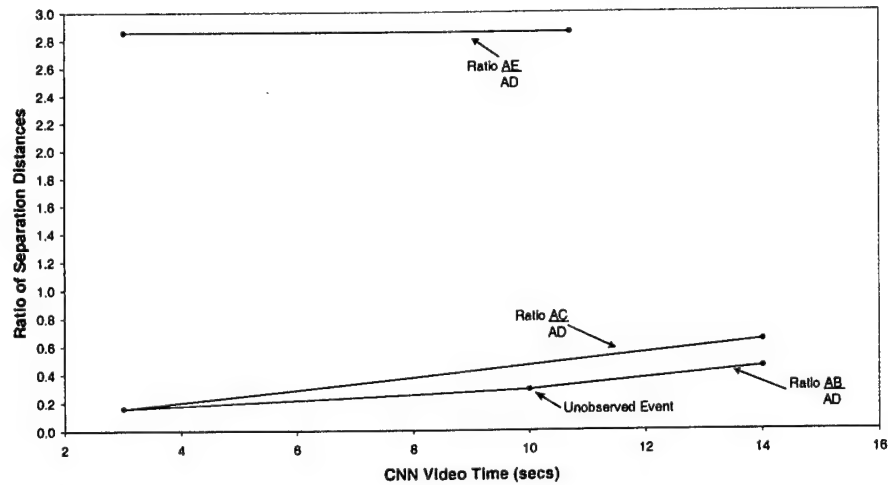
The relative angular separation of objects in terms of their percentage of the full video screen were calculated as a function of time. The relative spacing of A to E and A to D remained constant. Therefore, the ratio of the separation of A and E to the separation of A to D remains constant. The ratios of the other major objects C and B are shown with the distance A to D normalized. Note: F is not shown as it is close to E and remains in a fixed relative position.

14

Determination of Ballistic Coefficients From
Separation Distances

➢ Two Objects Which Are Closely Spaced and Slowly Separating
  ◆ Experiencing Approximately the Same Dynamic Pressure
  ◆ Assuming Constant Ballistic Coefficients (β) Relative
    Acceleration Is Constant

➢ Relative Intrack Motion Δx

$$\Delta x = g\,q\left[\frac{\beta_1 - \beta_2}{\beta_1\,\beta_2}\right]\frac{t^2}{2} + \left(\Delta V_{2/1}\right)_0 t + x_0$$

β = Ballistic Coefficient $\beta_1 > \beta_2$

t = time from point where relative velocity is $\left(\Delta V_{2/1}\right)_0$

x_0 = intrack separation when $t = 0$

15

The above chart shows the method for determining ballistic coefficients from the relative intrack separation distances of objects. The dynamic pressure q is slowly varying because absolute velocity and altitude (density) are nearly constant over a short period of time. The relative intrack motion can be established and hence the ballistic coefficient of one object can be derived if the other is known. The ballistic coefficient of the lead object has been derived from the tracking data. Likewise, the dynamic pressure is obtained from the lead object trajectory reconstruction.

A useful byproduct of the calculation is the derived separation time of the objects.

Determination of Ballistic Coefficients From Separation Distances (cont'd)

➢ Given Separation Distances and Reference Times x_1 at t_{CNN1} and x_2 at t_{CNN2}

$\Delta t = t_{CNN2} - t_{CNN1}$

t_s = separation time

$$t_s = \frac{\Delta t \left[1 + \sqrt{2 - \dfrac{x_2}{x_1}} \right]}{\dfrac{x_2}{x_1} - 1}$$

➢ $\dfrac{\beta_1 - \beta_2}{\beta_1 \beta_2} = \dfrac{2x_1}{g \, q \, t_s^2}$

THE AEROSPACE CORPORATION

16

Video

17

Views are taken at various CNN video times.

Time (secs)	Comment
1.2	Near First Acquisition
6.9	9 Initial Objects and 1 Secondary Object in View
12.4	Lead Object Point of Closest Approach
13.83	Lead Object at Palm Tree
23.7	Post Aerothermal Breakup of Lead Object

CNN Video At 1.2 Seconds

Copyright CNN, Used with Permission

THE AEROSPACE CORPORATION

18

Near first acquisition.

CNN Video At 6.9 Seconds (20803.2 GMT)

Copyright CNN
Used with Permission
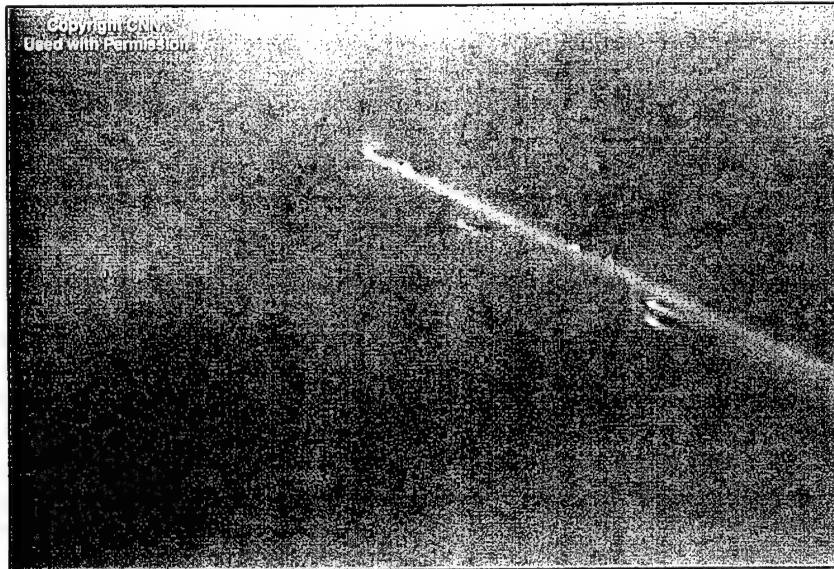
THE AEROSPACE
CORPORATION

19

Nine initial objects and one secondary object in view. See Page 20 for relative spacing.

Visible Objects at 6.9 Seconds
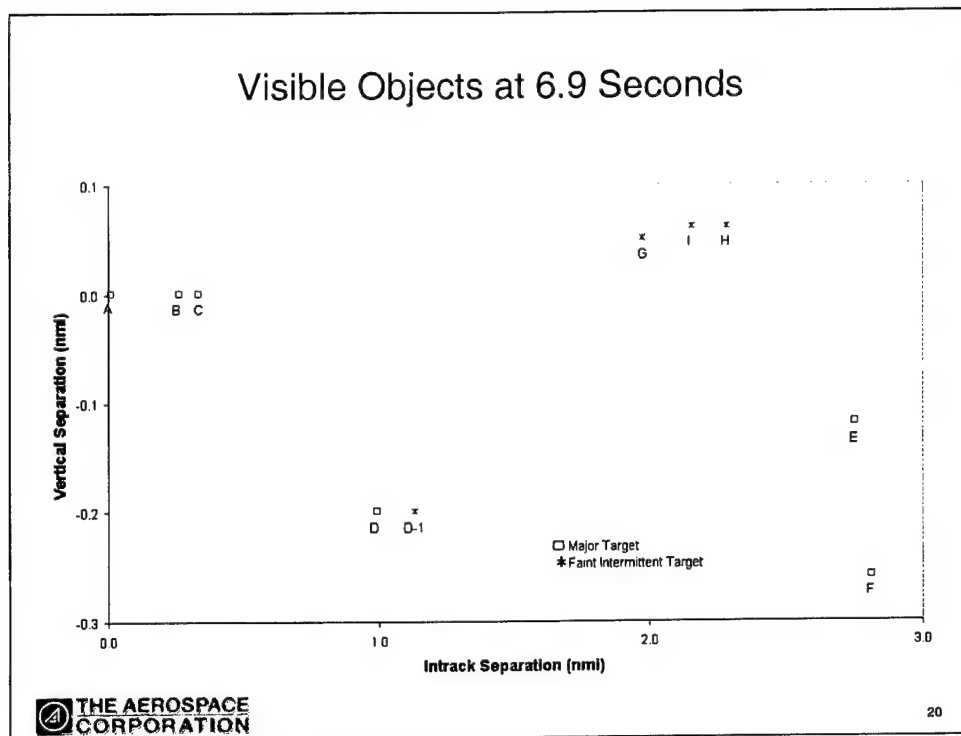
The identification of the 9 initial major objects visible at 6.9 seconds and their relative spacing intrack and radially are shown. The crosstrack displacement of the objects cannot be established.

The designation of Objects A through F is in order of their intrack position at this time. Objects G, H and I were designated in the order they were discovered. Objects with dash mark, A-1, C-1 and D-1 are sub-fragments of their parent object (i.e. A-1 comes off A).

CNN Video at 12.4 Seconds

Copyright CNN,
Used with Permission

THE AEROSPACE
CORPORATION

21

Lead Object A point of closest approach. Objects A, B, C and D in view.

CNN Video at 13.83 Seconds

Copyright CNN,
Used with Permission

22

Lead Object A at palm tree. Objects A, B, C and D in view.

CNN Video at 23.7 Seconds

Copyright CNN,
Used with Permission

THE AEROSPACE
CORPORATION

23
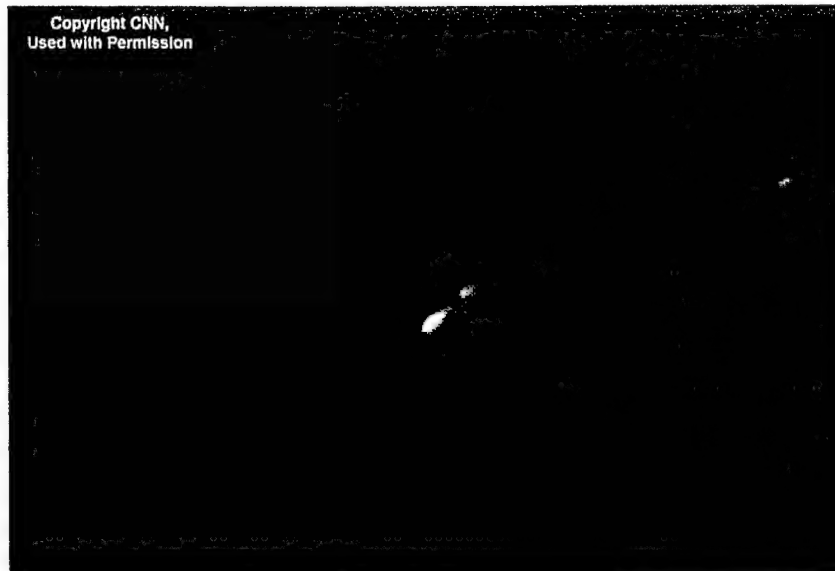
Post aerothermal breakup of lead Object A.

Object Summary

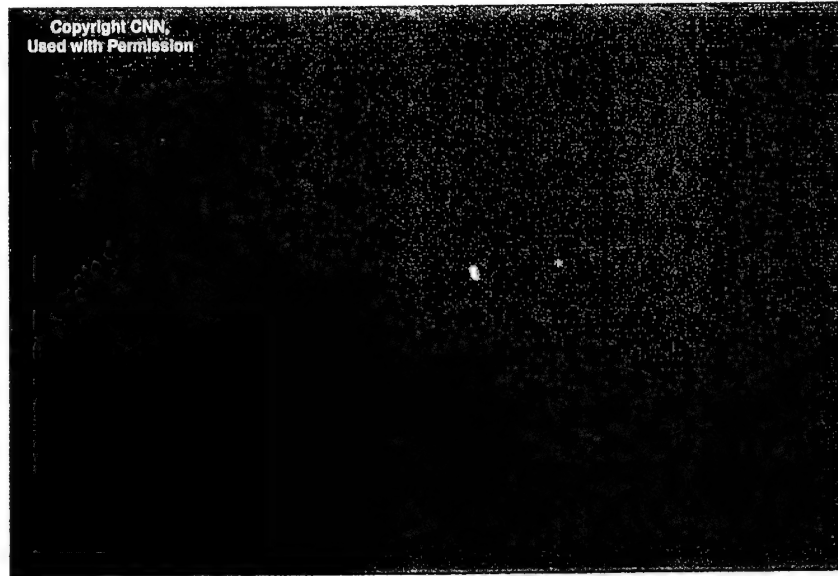| Object	Object Separated From	Separation Time* (T_{CNN} Video) Seconds	Ballistic Coefficient LB/FT²
A	MIR	Unknown	85
B/C	A	Estimate -1.0	≈40
B	B/C	3.0	60 (40 after 10 seconds)
C	B/C	3.0	40
D	MIR	Unknown	85
E	MIR	Unknown	85
F	MIR	Unknown	85
G	MIR	Unknown	?
H	MIR	Unknown	?
I	MIR	Unknown	120
A-1	A	7.3	3.5
D-1	D	2.0	25
C-1	C	11.9	.03 (Gas?)

*CNN Time Zero = 20796.3 Seconds GMT

24

An object summary with the separation time, derived ballistic coefficient and time of evolution is provided.

Objects B and C were connected to each other and to Object A one second prior to the start of the video. This estimate is based upon the separation rate observed during the video. The separation time is based upon the observed motion history.

The major Objects C through I as well as Object A separate at a time which is unknown from video information.

Secondary breakups A-1, D-1 and C-1 are observed and ballistic coefficients derived.

Object Video Tracking Summary

Object	Viewing Period Seconds	Loss of Picture	Observed Aerothermal Breakup
A	29	Clouds	Yes
B	27	Clouds	Yes
C	15	FOV	Yes
D	14	FOV	?
E	10.8	FOV	No
F	10.8	FOV	No
G	1.0	Dim Out	No
H	1.4	Dim Out	No
I	2.1	Dim Out	No
A-1	0.5	Dim Out	?
D-1	3.2	Dim Out	?
C-1	0.2	Dim Out	(Gas or Ablation Product?)

FOV – Out of Field of View

THE AEROSPACE CORPORATION

25

The table provides the tracking duration reason for loss of picture and whether indications of aerothermal (melting) breakup were observed. Objects A through F were viewed continuously until out of view. Lead Object A was viewed continuously as it was the object that the video ultimately concentrated on. Object B was observed almost as long but occasionally moved out of the FOV. Objects A and B were eventually obscured by clouds. The FOV was reduced to the point where Object C could no longer be viewed after 15 seconds. Aerothermal breakup was observed on Objects A, B and C prior to loss of picture.

Trailing Objects E and F moved out of the FOV before aerothermal breakup could be observed. Likewise, briefly viewed Objects G, H and I dimmed out without aerothermal breakup being observed.

Secondary Objects A-1 and D-1 dimmed out without any visual evidence of subsequent breakup. Object C-1 appeared to be gas or an ablation product indicating the beginning of melting at 11.9 seconds when it appeared.

Mechanical Separation of Compartments

➤ Objects D, E, F, G, H and I Have Radial And/or Crosstrack Displacements
  ◆ Lift
  ◆ Propulsive Decompression
➤ Objects D, E, F, G, H and I Trail the Lead Object A (1.0 → 2.75 nmi)
  ◆ Trailing Objects Have Equal or Higher Ballistic Coefficients Than Object A During Video (i.e., Keeping Pace or Gaining On Object A)
  ◆ Trailing Objects Upon Separation Experienced Higher Deceleration
    • Initial Broadside Attitude (Consistent With Lift)
    • Propulsive Decompression
➤ Initial Trailing Objects (D, E, F, G, H and I) Are The Radial Oriented Compartments of MIR

26

A mechanical separation of compartments prior to the CNN viewing period was evident. Trailing Objects D, E, F, G, H & I have radial and possibly crosstrack displacements (see Page 23). Trajectory studies have indicated that with objects of equal or similar ballistic coefficients radial displacement while in close proximity are possible only with aerodynamic lift and/or propulsive forces. Trailing Objects D through I trail the lead object from one nmi to 2.75 nmi. When observed in the video they have equal or higher ballistic coefficients (i.e. they are keeping pace or gaining on the lead object). Prior to the video coverage they had to have experienced higher decelerations than the lead object which may be due to higher drag through a broadside orientation or propulsive forces. The "spoke" or radially oriented compartments of MIR as indicated previously are broadside to the airstream during reentry. As these compartments separate from the center compartments they would be initially broadside producing high drag and lift forces. The pressurized compartments as they separate would provided propulsive decompression forces and perhaps more important an element of jet damping on the compartments. The jet damping would tend to slow the rotation rate buildup prior to tumbling. Tumbling motion would provide little net lift but the initial motion near broadside would produce lift over a brief period. It may be concluded that Objects D, E, F and I are radial components of MIR from their ballistic coefficients and radial offsets. Objects G and H are probably fragments from the radial compartments.

The excellent CNN video coverage of lead Object A allowed analysis of the fragments to be performed. The aerothermal breakup occurred 13 seconds into the video (20809.3 sec GMT) at an altitude of 37.75 nmi. Breakup of Object B was observed at about the same time but the intermittent coverage did not allow relative trajectory processing such as was performed for Object A. Object A prior to major aerothermal breakup experienced separation of a low ballistic coefficient object (3.5 lb/ft²). No subsequent fragmentation occurred indicating that the fragment could have been a low density object. No change in the ballistic coefficient of the parent Object A was observed implying the mass loss was minimal. While the fragment separation was probably structural in nature aerothermal effects cannot be ruled out.

Object C at 12 seconds (20808.3 sec GMT) exhibited an emission of an object of very low ballistic coefficient (0.03 lb/ft²) which was likely an ablation or melting effect. This event occurred at an altitude of 37.84 nmi less than 0.1 nmi above the initiation of lead Object A aerothermal breakup. Objects A, B and C were experiencing aerothermal breakup at the same time.

It should also be mentioned that an object separated from D two seconds into the video (20798.3 sec GMT) at an altitude of 38.4 nmi. The ballistic coefficient of the object was fairly high at 25 lb/ft² . No subsequent breakup of either Object D or its fragment D-1 were observed.

Aerothermal breakup likely occurred around 37.8 nmi but could have occurred as high as 38.4 nmi (Object D-1).

Aerothermal Breakup (cont'd)

➢ High Ballistic Coefficient Object (25 lb/ft^2) Separates From
Object D Two Seconds Into Video

H = 38.4 nmi

V_R = 23,853 ft/sec

q = 40.5 lb/ft^2 dynamic pressure

➢ Aerothermal Breakup

$T_{CNN} - 2 \rightarrow 13$ Seconds

$H \approx 37.8 \rightarrow 38.4$ nmi

28

Mir Configuration
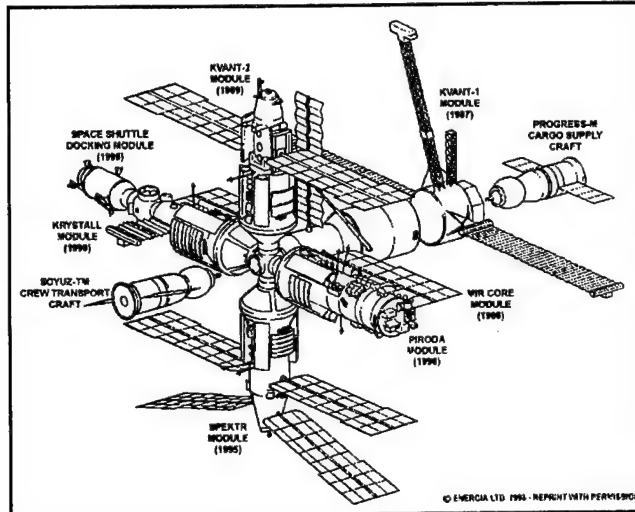
The radial objects (Krystall, Space Shuttle Docking Module, Piroda Module, Spektr Module, Kvant2) were likely the trajectory objects D, E, F, and I. Note Soyuz was absent during reentry. The central elements (MIR Core Module, Kvant1 Module and Progress Cargo Supply Craft) were probably the lead Objects A, B and C which separated from each other during an interval beginning one second before video coverage to 3 seconds after beginning of coverage, around 38.5 nmi.

Breakup Considerations

➤ Major Compartment Separation Took Place Prior to CNN Video Coverage (H=38.5 nmi)
   ◆ Alternate Coverage Suggests 41.1 → 41.6 nmi
   ◆ Dynamic Pressure 17.8 → 20.2 lb/ft²
   ◆ Event 54 → 63 Seconds Prior to CNN Video
➤ VAST Heating Equations (Predict Over Order of Magnitude Less Heating Than Traditional Convective Heating Equation)
   ◆ Prediction 3.2 → 3.4 BTU/FT² Sec
   ◆ Under Radiation Equilibrium Conditions Thin Aluminum Melts at 3.8 BTU/FT² Sec
      • Achieved at 40.7 nmi
      • 42 Seconds Before CNN Video
      • 54 Seconds Before Aerothermal Breakup
   ◆ Large Thermal Mass Delayed Extensive Aerothermal Breakup
➤ Objects Observed by CNN Have Likely Been Stripped of Externally Mounted Fixtures

THE AEROSPACE CORPORATION   30

The mechanical separation of the radial MIR modules occurred before CNN video coverage. There was some indication from other sources that some kind of event might have occurred 60 seconds earlier at an altitude between 41.1 and 41.6 nmi. VAST heating equations summarized on the next chart predict heating rates of 2.6 to 2.7 BTU/ft² sec at those altitudes. Those heating rates are insufficient to cause aerothermal breakup of aluminum. Aluminum was the primary external structural material. A thin aluminum structure under radiation equilibrium conditions (i.e., heat input matched by thermal radiation outwards) would reach melting temperatures at a heat input of 3.1 BTU/ft² sec (see Appendix A). This would occur at an altitude of 40.7 nmi some 54 seconds before observed aerothermal breakup. It is noted that the VAST equations predict heating rates an order of magnitude lower than traditional convective heating equations.

The large thermal mass of MIR likely accounted for the delay in aerothermal breakup. Aerothermal breakup occurs when the structural temperature approaches the material's melting temperature (see References 1 and 2). The MIR aerothermal demise is consistent with the VAST heating equations.

The solar arrays, mast, antennas and various other protrusions likely broke off or folded back to become ineffective as drag devices. (This behavior has been noted on a number of military reentries.)

VAST Empirical Heating Rates

➢ Stagnation Point Heating $(\dot{Q}_{STAG})$

$$\dot{Q}_{STAG} = 34.3 \left(\frac{\rho}{\rho_{SL}}\right)^{1/2} \left(\frac{V_R}{10,000}\right)^3 \text{ btu/ft}^2 \text{ sec}$$

ρ = Atmospheric Density

ρ_{SL} = Sea Level Atmospheric Density

V_R = Relative Velocity - ft/sec

➢ Side or Leeward Heating $(\dot{Q}_{SIDE})$

$(\dot{Q}_{SIDE})$ = 0.89 $(\dot{Q}_{STAG})$

➢ Effect of Radius

- No Increase for Most Radii
- For Radius < 2", Increase Heating by 40%

31

The heating equations were derived empirically and tested on experimental military satellite reentries. Details are found in Appendix A.

The VAST equations are consistent with the findings in References 3 through 6 which are associated with "strong shock" wave conditions.

Conclusion

➢ MIR Mechanically Separated Into Individual Modules
  • Probably Around 41.1 → 41.6 nmi

➢ Massive Aerothermal Breakup of the Leading Compartment Occurred at 37.8 nmi
  • 67 → 76 Seconds After the Possible Mechanical Separation Point

➢ VAST Aerothermal Heating Equations Consistent With Observed Breakup

➢ Ballistic Coefficients Consistent With Tumbling Compartments

➢ Nine Separate Objects Observed Early in CNN Video (Six Major, Three Minor)
  • Consistent With Eight Compartments (Including Progress)

THE AEROSPACE CORPORATION

32

Initially, MIR radial modules mechanically separated into individual modules probably between 41.1 and 41.6 nmi. The center modules mechanically separated around 38.5 nmi.

Aerothermal breakup consistent with the VAST heating equations (see Appendix A) occurred around 37.8 nmi. The derived ballistic coefficient of Objects A, B, C, D, E, F and I are consistent with tumbling components of MIR.

Aside from the mechanical separation of MIR into individual components, the reentry was a typical reentry with aerothermal breakup of an aluminum structure occurring at 37.8 nmi.

References

1. *Aerothermal Implications of VAST Breakup Sequence*, Aerospace Report No. TOR-2000(8504)-10, June 2000. Prepared by R. G. Stern, The Aerospace Corporation.

2. *Atmospheric Reentry History and Survival of a Large Solar Array*, Aerospace Report No. TOR-2001(8456)-1105, 01 August 2001. Prepared by R. G. Stern, The Aerospace Corporation.

3. *An Analytical Model of the Atmospheric Entry of Large Meteors and its Application to the Tunguska Event*, Lyne, J. E., Tauber, M. E., & Fought, R. M., The Journal of Geophysical Research, Vol. 101, No. E10, pp. 23207-23212, 1996.

4. *The Tunguska Event*, Lyne, J. E. & Tauber, M. E., Nature, Vol. 375, No. 6533, pp. 638-629, 1995.

5. *A Computer Model of the Atmospheric Trajectory of the Tunguska Object*, Lyne, J. E., Tauber, M. E., & Fought, R. M., invited presentation at the International Tunguska '96 Workshop, Bologna, Italy, July 15-17, 1996.

6. *An Analysis of the Tunguska Event*, Lyne, J. E. & Tauber, M. E., AIAA Paper 95-3477, presented at the 1995 AIAA Atmospheric Flight Mechanics Meeting , Baltimore, MD., August 1995.

7. *Satellite Thermal Control Handbook*, Spacecraft Thermal Department, The Aerospace Corporation, 1994

8. *Mir Reentry Breakup and Analysis*, Aerospace Report No. TOR-2002(9367)-1857, 01 July 2002. Prepared by W. P. Hallman, The Aerospace Corporation.

9. http://www.cnn.com/2001/TECH/space/03/23/williams.debrief/indes.ht

THE AEROSPACE CORPORATION

33

Appendix A

References 1 and 2 employed heating rate equations derived from the VAST reentry breakup sequence. The heating rate equations were based upon aluminum attaining a melting temperature under radiation equilibrium conditions. Radiation equilibrium conditions exist when the heat input to an object is equal to that radiated out. The above assumption is warranted since the rate of change of altitude and, hence, heating rate changes were very low in the vicinity of breakup where the thin aluminum monocoque structure approached the melting temperature.

The emissivity of the aluminum at melting was conservatively assumed to be unity. The result was that a higher than calculated heating rate was required to melt aluminum than would exist with a more realistic emissivity. The radiation heat emitted by a body is as follows:

$$\dot{Q} = \varepsilon \, \sigma \, T^4 \tag{1}$$

where:

$\dot{Q}$ = Heating rate btu/ft^2 sec

ε = Emissivity

σ = Stefan-Boltzman constant = 4.8×10^{-13} btu/ft^2 sec °R^4

T = Temperature °Rankine (1680°R Aluminum Melting Temperature)

If ε is assumed to be 1.0 then the heating rate at the aluminum melting temperature is:

$$\dot{Q} = (1.0) \, 4.8 \times 10^{-13} \, (1680)^4 = 3.82 \text{ btu/ft}^2 \text{ sec} \tag{2}$$

Free molecular heating rates commonly take the form:

$$\dot{Q}_{FMH} = K \left(\frac{\rho}{\rho_{SL}} \right)^{0.5} \left(\frac{V_R}{10000} \right)^3 = \text{Free molecular heating (btu/ft}^2 \text{ sec)} \tag{3}$$

where:

$$\frac{\rho}{\rho_{SL}} = \frac{\text{density at altitude}}{\text{density at sea level}}$$

V_R = Relative Velocity ft/sec

From Reference 1 for VAST, the K for $\dot{Q} = 3.82$ would be 42.9

or:

$$\dot{Q} = 42.9 \left(\frac{\rho}{\rho_{SL}} \right)^{0.5} \left(\frac{V_R}{10000} \right)^3 \text{ btu/ft}^2 \text{ sec} \tag{4}$$

In both References 1 and 2, Eq. (3) was used to predict the flight conditions to melt aluminum. Eq. (3) for aluminum under radiation equilibrium conditions should attain 3.82 btu/ft^2 sec. The aluminum surface for the outer structure of the vehicles used in the VAST experiments was clear-anodized aluminum and the emissivity should be 0.8 (Reference 7).

For determination of the surface temperature for other materials and surface finishes, the heating rate determined by Eq. (2) should be modified as follows:

$$\dot{Q} = (.8)4.8 x 10^{-13} (1680)^4 = 3.056 \text{ btu/ft}^2 \text{ sec} \tag{5}$$

K of Eq. (3) is then modified to reflect the lower heating rate of Eq. (5) by the ratios of emissivity of 1.0 and 0.8. Eq. (4) then becomes:

$$\dot{Q} = 34.32 \left(\frac{\rho}{\rho_{SL}} \right)^{0.5} \left(\frac{V_R}{10000} \right)^3 \tag{6}$$

Using the above relationship and Eq. (1) with an appropriate emissivity, a temperature can be determined from the heating rate of Eq. (6).

The factors presented in Reference 1 for leeside heating (.89) and for small radii (1.4) are not affected and are presented below:

Table A-1: VAST Empirical Heating Rates

Stagnation Point Heating $\left(\dot{Q}_{STAG} \right)$

$$\dot{Q}_{STAG} = 34.3 \left(\frac{\rho}{\rho_{SL}} \right)^{0.5} \left(\frac{V_R}{10000} \right)^3 \text{ btu/ft}^2 \text{ sec}$$

ρ = Atmospheric Density

ρ_{SL} = Sea Level Atmospheric Density

V_R = Relative Velocity - ft/sec

Side or Leeward Heating $\left(\dot{Q}_{SIDE} \right)$

$$\dot{Q}_{SIDE} = 0.89 \left(\dot{Q}_{STAG} \right)$$

Effect of Radius

No Increase for Most Radii

For Radius < 2", <u>Increase</u> Heating by 40%

The above heating relationships are very similar to the strong shock phenomena analyzed in References 3-6. The heating rates associated with the above equations are generally an order of magnitude less than traditional convective heating equations. Therefore, the "strong shock" effect increases the survivability of debris from satellite reentry and greatly lowers the breakup altitude. No criteria is provided for determining if

the heating associated with "strong shock" is appropriate. It is noted, however, that items less than 1 ft. wide have survived and have had "strong shock" protection.

The survivability of various materials entering under "strong shock" conditions may be surmised in Table A-2. The heating rate to achieve a melting temperature under radiation equilibrium conditions is determined. For other than thin walled or low thermal capacity structures entering with shallow flight path angles (where the change in heating rate with altitude is small), the actual temperature will lag the equilibrium temperature and will therefore be lower.

Table A-2

Material	Surface	Melting Temperature (°R)	Emissivity	$\dot{Q}_{CRIT}$ Radiation Equilibrium Heating Rate for Melting (btu/ft² sec)	*β_{CRIT} Critical Ballistic Coefficient (lb/ft²)
Aluminum	Clear Anodized	1680	0.8	3.06	16
↓	Oxidized	↓	0.25	0.96	5
Titanium	Bare	3494	0.55	39.3	≈ 400
Steel	Sheet	3100	0.6	26.6	≈ 260
↓	Oxidized	↓	0.8 – 0.9	35.4 – 39.9	≈ 400
Glass	---	3060	0.89	37.5	≈ 400

*β Required to Achieve Melting From Polar Orbit Decay

The critical heating rate, which matches the melting temperature and emissivity for specific materials, is provided in Table A-2. The corresponding minimum ballistic coefficient for the object to achieve the critical heating rate is also provided. The minimum ballistic coefficient assumes decay from a polar orbit.

Variations in the minimum ballistic coefficient will exist for actively deboosted satellites and orbits. Active deboost from a high energy orbit would require a separate evaluation. The heating rate equations of Table A-1 have been shown to be valid for velocities up to 32,000 fps and flight path angles to seven degrees. Table A-2 demonstrates the almost certain thermal survivability of steel, titanium and glass under "strong shock" conditions, since ballistic coefficients of several hundred lb/ft² are uncharacteristic of debris. The load factor at peak heating is relatively low, on the order of several G's. Peak load conditions are experienced well after peak heating at which point the object's temperature is declining but still elevated. Some structural deformation will likely occur but the mass of the object should survive. Low ballistic coefficients (with respect to the critical value) will have peak temperatures less than melting, insuring survival. Aluminum panels (Reference 2), countless titanium propellant tanks, and glass objects have survived reentry. Most titanium tanks and glass objects (W/C$_D$A ≈ 55 lb/ft²) survive almost unscathed.